Oxidative corrosion resistance of a Cr Fe Ni composition spread alloy film (CSAF) in dry air

Camille Ferris, Nicholas Golio, Hervé Martinez, Andrew J Gellman

To cite this version:

Camille Ferris, Nicholas Golio, Hervé Martinez, Andrew J Gellman. Oxidative corrosion resistance of a Cr Fe Ni composition spread alloy film (CSAF) in dry air. Applied Surface Science, 2024, 669, pp.160391. 10.1016/j.apsusc.2024.160391 . hal-04613754

HAL Id: hal-04613754

https://univ-pau.hal.science/hal-04613754v1

Submitted on 17 Jun 2024

Applied Surface Science 669 (2024) 160391

Contents lists available at ScienceDirect

Applied Surface Science

journal homepage: www.elsevier.com/locate/apsusc

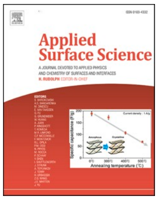

Full Length Article

Oxidative corrosion resistance of a $Cr_xFe_yNi_{1-x-y}$ composition spread alloy film (CSAF) in dry air

Camille Ferris[a], Nicholas Golio[a], Hervé Martinez[a,b], Andrew J. Gellman[c,d,*]

[a] Université de Pau et des Pays de l'Adour, E2S UPPA, CNRS, IPREM, Pau, France
[b] Ecole Centrale Casablanca, Centre de Recherche Systèmes Complexes et Interactions, Bouskoura, Morocco
[c] Department of Chemical Engineering, Carnegie Mellon University, Pittsburgh, PA, United States
[d] W.E. Scott Institute for Energy Innovation, Carnegie Mellon University, Pittsburgh, PA, United States

ARTICLE INFO

Keywords:
Chromium
Iron
Nickel
Thin film alloys
Oxidation resistance
X-ray photoelectron spectroscopy

ABSTRACT

Composition Spread Alloy Films (CSAFs) were used to study the resistance to oxidative corrosion of $Cr_xFe_yNi_{1-x-y}$ alloys in dry air and determine the critical Cr composition, x^*_{Cr}, necessary to prevent bulk oxidation. $Cr_xFe_yNi_{1-x-y}$ CSAFs were made using physical vapor deposition (PVD) and then oxidized in dry air between 100 – 500 °C for periods of 1 h. A sharp passivation boundary was observed at 300 °C separating alloys showing evidence of heavy oxidation from Cr-rich alloys that were passivated. X-ray photoelectron spectroscopy (XPS) depth profiling was used to measure the extent of oxidation and penetration depth of the oxide layer on either side of the passivation boundary. XPS measurements confirmed the presence of a critical Cr composition, x^*_{Cr}, ranging from 18 to 26 at. %. For alloys with $x_{Cr} \geq x^*_{Cr}$, a sufficiently thick passivating layer of oxidized Cr, $Cr^{(ox)}$, had formed on the top surface preventing the oxidative corrosion of either Fe or Ni. On the other hand, when $x_{Cr} < x^*_{Cr}$, bulk oxidation was observed, with appreciable $Fe^{(ox)}$ and/or $Ni^{(ox)}$ measured on the surface and often penetrating through the entire alloy film thickness. The trajectory of x^*_{Cr} plotted within $Cr_xFe_yNi_{1-x-y}$ composition space supports the trend towards using higher Cr-content stainless steel grades in harsh oxidative environments.

1. Introduction

The use of metal alloys is widespread in society, with applications in modern technologies ranging from structural materials to manufacturing. Designing alloys that possess mechanical and/or chemical properties superior to those of their constituent metals involves fine-tuning their functional properties within composition space. These properties arise from the complex interactions of alloy components with one another and with their local environment.

In the field of structural materials, "superalloys" based on Ni_xFe_{1-x} alloys modified by a variety of additive components are particularly interesting. These materials have extremely high performance and durability, and are carefully designed for their mechanical, chemical, and economic advantages [1–5]. The functional properties of alloys and superalloys often depend significantly on their atomic composition. Optimization of the alloy composition is often a key factor in achieving its desired performance, such as for oxidation resistance [6,7]. Thus, the development of durable alloys for structural applications requires improving our understanding of their oxidation resistance, especially in high temperature environments [6–8].

Stainless steels, such as 304L, fall within the $Cr_xFe_yNi_{1-x-y}$ composition subspace of $Co_xCr_yFe_zNi_{1-x-y-z}$ superalloys and are used in numerous engineering applications. The oxidation resistance of alloys like stainless steel 304L arises from the presence of Cr, which creates a passivation layer consisting of a mixture of Cr oxides and Cr hydroxides over the surface of the material [9–13]. The passivation layer protects against oxidative corrosion of the alloy since it prevents O_2 in the gas phase from penetrating beneath the oxidized Cr layer, preserving the bulk in a metallic state [14–17]. Due to the high cost of Co relative to the other elements in the $Co_xCr_yFe_zNi_{1-x-y-z}$ superalloy, exploration of the corrosion behavior of ternary alloys consisting only of $Cr_xFe_yNi_{1-x-y}$ is also valuable [13].

The ability of transition metals to passivate oxidative corrosion is based on a parabolic law for the rate of oxide film growth or thickening, as presented by Wagner [18]. In thin oxide films on metal surfaces, the rate of oxide film thickening (i.e., oxidation) is inversely proportional to

---

[*] Corresponding author at: Department of Chemical Engineering, Carnegie Mellon University, Pittsburgh, PA, United States.
E-mail address: gellman@cmu.edu (A.J. Gellman).

https://doi.org/10.1016/j.apsusc.2024.160391
Received 15 March 2024; Received in revised form 17 May 2024; Accepted 24 May 2024

the thickness of the oxide layer. The thickening is the result of ion transport across the thin oxide film under the driving force of an electric field. Oxygen ions can diffuse into the material and/or metal ions can diffuse out to the surface leading to the progressive thickening of the oxide layer. Since oxide layers are effective diffusion barriers, they can passivate against oxidative corrosion once they become sufficiently thick and laterally continuous across the surface. In multicomponent alloys, one or more components can act as passivating agents, preventing the oxidative corrosion of the bulk material. In the passivation mechanism attributed to Wagner, the metal component more thermodynamically prone to oxidation reacts with O atoms that have diffused into the bulk of the alloy. However, if the diffusion of metal atoms to the surface of the alloy is greater than the rate of O atom diffusion into the alloy, then the oxide forms at the surface and not within the bulk of the material. Once a contiguous oxide film forms across the surface, it acts as a barrier to further diffusion in either direction and the bulk is considered passivated. This passivation mechanism suggests that within multicomponent alloy systems, like $Cr_xFe_yNi_{1-x-y}$, there exists a critical bulk concentration, x^*, for components like Cr that are capable of forming passivating oxide films. When the Cr composition of $Cr_xFe_yNi_{1-x-y}$ alloys is greater than or equal to the critical Cr concentration (i.e., $x_{Cr} \geq x^*_{Cr}$), a passivating oxide layer, $Cr^{(ox)}$, is formed that prevents oxidative corrosion in the bulk.

The ability of elements like Cr and Co to form passivating oxide layers depends on their affinity for reaction with O_2 and/or other oxidizing gases present in their operating environment. Neglecting entropy differences between metallic and oxidized species, the oxidation affinity of an element is governed thermodynamically by its standard enthalpy of oxide formation, ΔH^0_f. The oxidation affinity increases for more negative (i.e., exothermic) values of ΔH^0_f. Thus, in an alloy system where several constituent elements are present, components with the most negative ΔH^0_f will preferentially oxidize to minimize the free energy of the system. Similarly, when a constituent element, such as Cr, possesses several different oxidation states, for example, Cr_2O_3 and CrO_3, it is expected that the oxide with the most exothermic ΔH^0_f will be dominant. The relevant Cr, Fe, and Ni oxides ($Cr^{(ox)}$, $Fe^{(ox)}$, and $Ni^{(ox)}$, respectively) along with their standard enthalpies of oxide formation, ΔH^0_f, are shown in Table 1. From comparing the values of ΔH^0_f in Table 1, the oxidation of $Cr_xFe_yNi_{1-x-y}$ alloys in dry air would initially yield the formation of Cr_2O_3 and Fe_3O_4 since the values of ΔH^0_f are similar and significantly more exothermic than ΔH^0_f for the other oxide species.

Ternary $Cr_xFe_yNi_{1-x-y}$ composition space provides a rich landscape over which to tune the functional properties of alloys with high engineering potential. In addition to the corrosion protection offered by Cr, increasing the Fe content decreases the raw materials cost while simultaneously increasing the melting point. On the other hand, a high enough Ni concentration must be maintained to induce the formation of a mechanically robust, austenitic matrix structure [23–26]. Therefore, careful measurements across $Cr_xFe_yNi_{1-x-y}$ composition space reveal the inherent trade-offs in functional properties resulting from different combinations of the constituent elements.

Table 1
ΔH^0_f for the relevant oxides in the $Cr_xFe_yNi_{1-x-y}$ system.

Oxide Species	ΔH^0_f(kJ/mol) [19–22]
$Cr^{(ox)}$	
Cr_2O_3	−1139.7
CrO_3	−589.5
$Fe^{(ox)}$	
FeO	−272.0
Fe_2O_3	−824.2
Fe_3O_4	−1118.4
$Ni^{(ox)}$	
NiO	−239.7

Traditional exploration of alloy properties across composition space requires the preparation and characterization of a large set of discrete, single-composition samples. The time and cost investment required to characterize composition space comprehensively with high resolution is prohibitive, especially as the number of components increases. Measurements of alloy properties can be greatly accelerated through the use of high-throughput methods based on a materials library. Composition Spread Alloy Films (CSAFs) are materials libraries which span composition space continuously. When coupled with rapid, spatially resolved characterization techniques, CSAFs allow efficient mapping of alloy properties across binary or ternary composition space in a single experiment. Such high-throughput methods have been used increasingly in the study of a wide range of problems in materials and surface science [27–32].

High-throughput studies using CSAFs have already been implemented in studying the corrosion resistance of various alloy systems [33–39]. Generally, this methodology involves exposure of the initially clean CSAF to a given set of oxidation conditions, at various temperatures and partial pressures of ambient O_2 and/or other oxidizing species, and then measuring the extent of oxidation as a function of alloy composition. In this work, $Cr_xFe_yNi_{1-x-y}$ CSAFs spanning all of ternary composition space (i.e., $x = 0 \rightarrow 1, y = 0 \rightarrow 1 - x$) were deposited onto polycrystalline Mo substrates and used for the high-throughput characterization of their resistance to oxidative corrosion in dry air (i.e., 20 % O_2 in N_2) as a function of temperature. The goal was first to identify an oxidation temperature that would reveal differences across the CSAF in the extent of oxidative corrosion resistance. Once passivation boundaries across the film were identified, depth profiles were obtained at CSAF compositions where the oxidative corrosion behavior changed abruptly. Depth profiles showing the penetration of oxides into the material at known bulk compositions allowed us to identify the critical Cr composition, x^*_{Cr}, required to passivate the oxidative corrosion of $Cr_xFe_yNi_{1-x-y}$ alloys. The trajectory of x^*_{Cr} was then mapped through ternary composition space.

2. Experimental

2.1. CSAF preparation

The CSAF samples were prepared on polished $14 \times 14 \times 3$ mm^3 Mo substrates (Valley Design Corp.) by physical vapor deposition of Cr, Fe, and Ni using a rotatable shadow mask CSAF deposition tool that has been described in detail previously [40,41]. The Cr, Fe, and Ni deposition rates from three independent electron beam evaporation sources were controlled by their heating power and were calibrated using a quartz crystal microbalance (QCM). The film thickness of each component was controlled by the deposition time and reached a combined total thickness of $\sim$ 60 nm uniformly across the surface. A plot of the total film thickness before oxidation of the $Cr_xFe_yNi_{1-x-y}$ CSAF in Fig. 1 can be found in Figure S1 of the Supporting Information. The orientation of the three shadow masks 120° from one another resulted in flux gradients of Cr, Fe, and Ni across the substrate. This yielded a triangular area over the center of the Mo substrate containing ternary composition space, $Cr_xFe_yNi_{1-x-y}$. The edges of this triangle contain alloys spanning the three binary composition spaces, Cr_xFe_{1-x}, Cr_xNi_{1-x}, and Fe_xNi_{1-x}. At the vertices of the triangle are the pure components.

2.2. CSAF characterization

Energy dispersive X-ray spectroscopy (EDX) of the $Cr_xFe_yNi_{1-x-y}$ CSAF was performed in a Tescan VEGA3 scanning electron microscope (SEM) in order to spatially map the bulk alloy composition and thickness versus position across the substrate. The CSAF was positioned by an automated stage, allowing analysis on a grid of 13×13 evenly spaced measurement

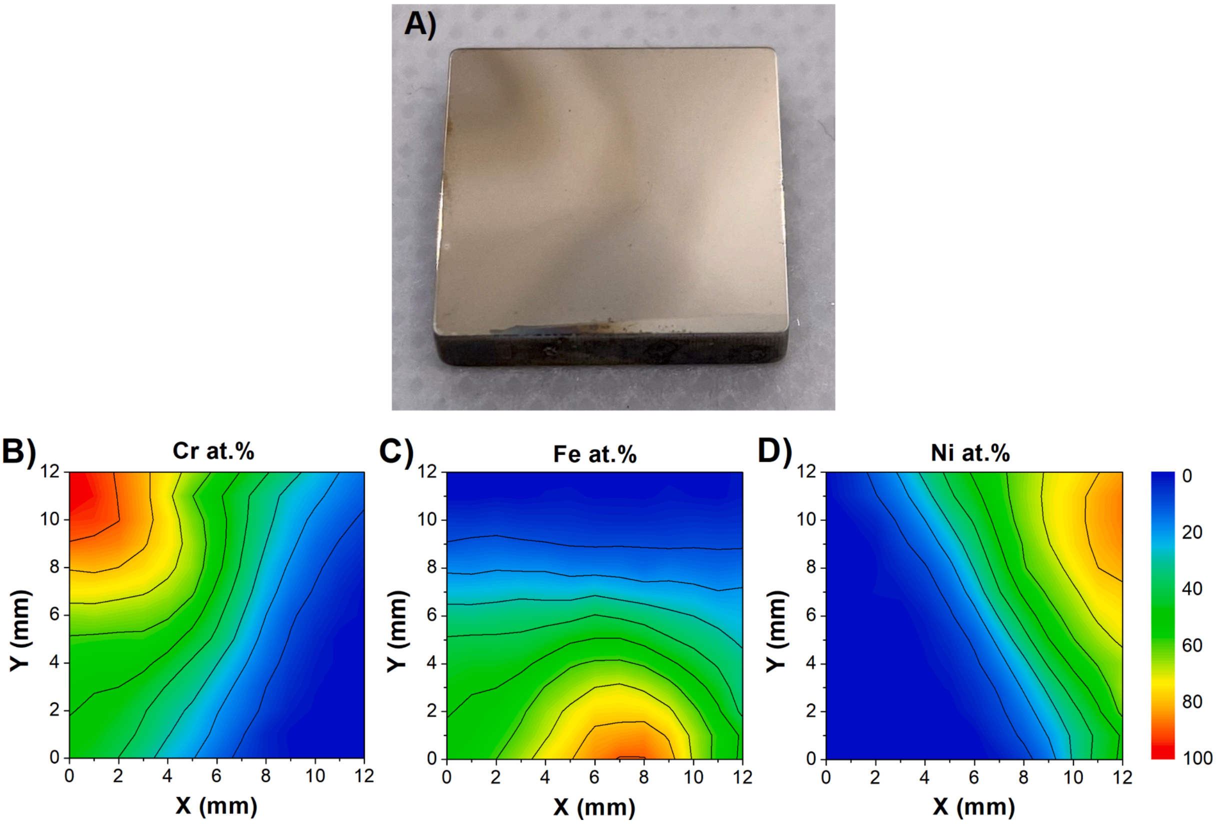

Fig. 1. **A)** Image of the $Cr_xFe_yNi_{1\text{-}x\text{-}y}$ CSAF as deposited on the 14 × 14 × 3 mm^3 polished Mo substrate. Note that there is a small region of bare Mo at the bottom edge of the film which resulted from the substrate being partially shielded during the deposition. **B)** — **D)** Atomic concentration maps of bulk Cr, Fe, and Ni as determined by EDX mapping across a 13 × 13 point grid spanning the 12 × 12 mm^2 area at the center of the Mo substrate. The entire ternary composition space is contained on the CSAF.

points spanning the 12 × 12 mm^2 area at the center of the substrate. The electron beam energy was set to 20 keV and the EDX scan area of each analysis point was 50 × 50 μm^2. Each measurement consisted of a scan from 0 – 20 keV since it spanned the range containing all of the characteristic X-ray energies emitted from Cr, Fe, Ni, and Mo [42]. The bulk alloy composition corresponding to each EDX spectrum was quantified using the Oxford Instruments INCA ThinFilmID^{TM} software package, which accounts for the morphology of a thin $Cr_xFe_yNi_{1\text{-}x\text{-}y}$ film deposited on a Mo substrate. The overall film thickness at each point was calculated by comparing the Cr, Fe, and Ni signal intensities at each measurement point with those of a Ni reference material.

2.3. Oxidation and visual analysis of $Cr_xFe_yNi_{1\text{-}x\text{-}y}$ CSAFs

Oxidation of the $Cr_xFe_yNi_{1\text{-}x\text{-}y}$ CSAFs was performed by flowing dry air (ALPHAGAS^{TM} 1 Air, Air Liquide) composed of 20 % O_2 in N_2 through an 80-mm diameter quartz tube furnace (OTF-1200X, MTI Corporation) with the CSAF loaded inside a quartz boat. The flow rate of dry air was controlled using a mass flow controller (EQ-GSL-LCD, MTI Corporation) set to the maximum flow rate of 500 mL/min to minimize the back-diffusion of ambient, humid air into the furnace. The water concentration in the tube furnace was monitored continuously using a humidity monitor and was always < 50 ppm throughout the course of the experiments. After establishing the flow of dry air, the furnace was pre-heated to the desired oxidation temperature between 100–500 °C for at least 30 min before loading the quartz boat containing the CSAF. After 1 h of oxidation, the quartz boat was removed from the tube furnace and placed on a ceramic plate in ambient air to rapidly cool the CSAF (<5 min) and quench the oxidation.

Once completely cooled, visual analysis of the oxidative corrosion across the CSAF was performed by taking photos of the surface to identify the boundaries between regions exhibiting different resistance to oxidative corrosion. To ensure that the lighting in each photo was uniform, the CSAF was placed into a photo light box (PULUZ®) containing LEDs that surrounded the sample and illuminated the surface with bright light. Due to the high reflectivity of the metallic surface, all photos were taken at a slight angle with respect to the surface normal to prevent the appearance of the camera in the image. The images of the oxidized CSAF surface obtained after 1 h of oxidative corrosion in dry air revealed the real-space locations of visually distinct boundaries between alloy compositions exhibiting different oxidative corrosion resistance. The visual boundary seen in these images is mapped onto composition space by interpolating the bulk composition maps obtained by EDX. Visual analysis in combination with spectroscopic characterization techniques enabled determination of the trajectory of the critical Cr composition, x_{Cr}^*, in $Cr_xFe_yNi_{1\text{-}x\text{-}y}$ composition space.

2.4. XPS characterization and depth profiling of the oxidized $Cr_xFe_yNi_{1\text{-}x\text{-}y}$ CSAF

Depth profiling through the CSAF was performed using X-ray photoelectron spectroscopy (XPS). XPS depth profiling is a destructive technique involving alternating cycles of XPS measurements and removal by Ar^+ etching of surface material from an area (1.2 × 1.2 mm^2) larger than the XPS beam diameter (200 μm). Alternating between removing thin layers of material and performing surface sensitive XPS measurements of alloy composition allows the composition of the film to be determined as a function of the depth into the film. By performing depth profiling until the appearance of the Mo substrate in the XPS spectra (i.e., the point at which the deposited film is completely removed), we obtained piecewise reconstructions of the entire film thickness at the analysis sites. It is important to note that Ar^+ depth profiling can lead to systematic underestimation of the extent of oxidation due to partial reduction of the surface caused by preferentially etching lighter elements (i.e., O) at a faster rate than heavier elements (i.e., transition metals). While we acknowledge, therefore, that the exact ratio of oxide to metallic components determined by this technique includes some systematic error [43–50], we assume that the difference in the etching rate of oxide species is negligible and thus, a semi-quantitative and comparative analysis between oxides and transition metals can still be performed.

The XPS depth profiling experiments were performed using a Thermo Scientific™ ESCALAB 250Xi instrument (Al K_α source) with a hemispherical energy analyzer and an X-ray spot diameter of 200 μm. Survey scans across a binding energy range of 0–1400 eV with a 1 eV step size, 140 ms dwell time, and 20 eV pass energy were used to confirm that no unexpected chemical species were present on the CSAF. Subsequent scans used for quantification during depth profiling were obtained over 20–40 eV ranges encompassing the non-overlapping Cr *2p*, Fe *2p*, Ni *2p*, O *1s*, and Mo *3d* peaks. The C *1s* peak was also collected to ensure that the initial carbon contamination at the surface disappeared after the first few etching cycles. Scans of the peaks corresponding to Cr, Fe, and Ni were performed with a 0.1 eV step size, 140 ms dwell time, and 20 eV pass energy, however, the dwell time was reduced to 100 ms for the O and C scans and 50 ms for Mo to reduce the overall experiment time. Between each set of XPS measurements, the CSAF was excavated across a targeted area of 1.2 × 1.2 mm^2 by rastering a focused monoatomic Ar^+ beam operated at 3 kV and 1 μA. Inside each square etched area, XPS measurements were taken at 5 analysis points equally spaced along the diagonal of the excavated region.

CasaXPS processing software was used to subtract XPS backgrounds (using the “Shirley” background unless the signal was weak enough to warrant “Linear”), fit peaks, and calculate peak areas. The transition metal orbital spectra for Cr $2p_{3/2}$, Fe $2p_{1/2}$, Ni $2p_{3/2}$, and Mo $3d_{5/2}$ were used for the analysis to avoid any overlap between peaks. In particular, the use of the Fe $2p_{1/2}$ orbital was necessary to avoid overlap with the Ni *LMM* Auger transition which occurs in the same binding energy range as Fe $2p_{3/2}$. Comparison of quantification using Fe $2p_{3/2}$ and Fe $2p_{1/2}$ on samples not containing Ni showed a variation of only ~3 at.%, which lies within the uncertainty of the measurement.

Oxide components of the transition metal peaks were fit using a fixed 30 % Gaussian/Lorentzian shape, while the metallic components were fit using reference spectra collected with the same analyzer settings for commercial samples of pure Cr, Fe, and Ni (NEYCO HEF® photonics) that had been sufficiently Ar^+ etched so that they exposed clean surfaces. Scofield sensitivity factors were used to scale the peak areas and determine the relative atomic composition of each component. In cases where both oxidized and metallic states of one of the constituent metals were present, XPS fitting was performed by constraining the FWHM of the metallic reference spectra between 0.9 and 1.1 and its peak position was constrained to lie at lower binding energy than the oxide components. Further assignment of the oxide peaks to specific oxidation states was not attempted.

3. Results

3.1. Characterization of $Cr_xFe_yNi_{1\text{-}x\text{-}y}$ CSAFs composition gradients

A thorough quantification of the alloy composition distribution across the CSAF is required for transformation of real-space analysis locations on the film into bulk alloy compositions. EDX was used to map $Cr_xFe_yNi_{1\text{-}x\text{-}y}$ composition across a 12 × 12 mm^2 region using a grid of 13 × 13 points with 1 mm spacing centered on the CSAF. Fig. 1A shows a photograph of a $Cr_xFe_yNi_{1\text{-}x\text{-}y}$ CSAF taken after deposition. Fig. 1B through 1D show the bulk alloy composition of Cr, Fe, and Ni in real space as determined by EDX. The maps in Fig. 1B through 1D can be used to find the alloy composition at any arbitrary point on the CSAF.

3.2. Visual inspection of CSAF oxidative corrosion in dry air

Visual inspection was used to identify the temperatures over which the resistance to oxidative corrosion of $Cr_xFe_yNi_{1\text{-}x\text{-}y}$ alloys in dry air is particularly interesting. Oxidation was performed at temperatures spanning the range $T = 100\text{–}500\ ^\circ C$ using a second CSAF, shown in Fig. 2. Fig. 2A through F show photographs of the second $Cr_xFe_yNi_{1\text{-}x\text{-}y}$ CSAF before and after sequential oxidation in dry air from 100–500 °C for 1 h. Note that despite being nearly identical in composition to the CSAF in Fig. 1A, the CSAF in Fig. 2A has darker coloration than the CSAF shown in Fig. 1A. This is attributed to a higher background oxygen pressure present during preparation of the second CSAF. Nonetheless, visual analysis of its subsequent oxidation in dry air allowed us to identify trends across $Cr_xFe_yNi_{1\text{-}x\text{-}y}$ composition space. These trends informed our treatment of the CSAF in Fig. 1A.

Visual analysis of the oxidative corrosion of the $Cr_xFe_yNi_{1\text{-}x\text{-}y}$ CSAF was performed using a photo light box to ensure that all of the photographs in Fig. 2 were taken from the same angle and with the same lighting conditions. The top row of Fig. 2 shows that the CSAF appears virtually unchanged except for some darkening in the Fe-rich region of the film after exposure to dry air for 1 h at 100 °C and 200 °C. The most interesting visual change to the film occurred after 1 h exposure to dry air at 300 °C. This treatment resulted in a blue and reddish-brown oxidative corrosion band that appeared in the region of high Fe composition and extended into $Fe_xNi_{1\text{-}x}$ binary alloy space. It is clear that there is a sharp boundary, marked by the dashed white line in Fig. 2D, separating a substantially oxidized region that appears in the lower right corner of the film after 300 °C from the rest of the CSAF, which appears unchanged. The sharp boundary that delineates heavily oxidized alloys from seemingly passivated alloys follows a similar trajectory to the contours of Cr composition shown in Fig. 1B. The relationship between the boundary and the contours of constant Cr composition suggests that the Cr composition of $Cr_xFe_yNi_{1\text{-}x\text{-}y}$ alloys is the most significant factor influencing their oxidative corrosion resistance.

Fig. 2E shows that further oxidation of the CSAF at 400 °C broadens the area experiencing oxidative corrosion into the Ni-rich region at the upper right edge of the film, but does not appreciably shift the passivation boundary established after oxidation at 300 °C. Only after further oxidation of the film at 500 °C (Fig. 2F) do the previously passivated alloys rich in Cr show visual evidence of oxidative corrosion in the form of blue, orange, and yellow patches to the left of the passivation boundary. Thus, the oxidative corrosion resistance exhibited by Cr-rich alloys after dry air exposure at 300 °C and 400 °C appears to break down once the temperature reaches 500 °C.

From visual inspection of the oxidative corrosion patterns in Fig. 2, we identify that the passivation boundary separating extensively oxidized alloys from passivated alloys first appears at 300 °C. Thus, dry air oxidation at 300 °C was chosen to be the most appropriate temperature for further study of the oxidative corrosion resistance of $Cr_xFe_yNi_{1\text{-}x\text{-}y}$ alloys. Subsequent analysis of the CSAF shown in Fig. 1A was used to characterize the oxidative corrosion resistance of $Cr_xFe_yNi_{1\text{-}x\text{-}y}$ alloys at 300 °C using XPS depth profiling.

3.3. XPS depth profiling across the passivation boundary

The $Cr_xFe_yNi_{1\text{-}x\text{-}y}$ CSAF in Fig. 1A was oxidized in dry air at 300 °C for 1 h. Images taken before and after oxidation are shown in Fig. 3A and B, respectively, with the overlaid black triangles demarcating the region of ternary composition space with the pure components labelled at the vertices. The dashed white line drawn on top of the oxidized CSAF in Fig. 3B delineates the sharp transition between alloys showing strong visual evidence of oxidative corrosion to the right and the alloys where oxidative corrosion was passivated to the left. The visual oxidative corrosion pattern shown in Fig. 3B is consistent with the one obtained at the same temperature on the second CSAF in Fig. 2D in the sense that

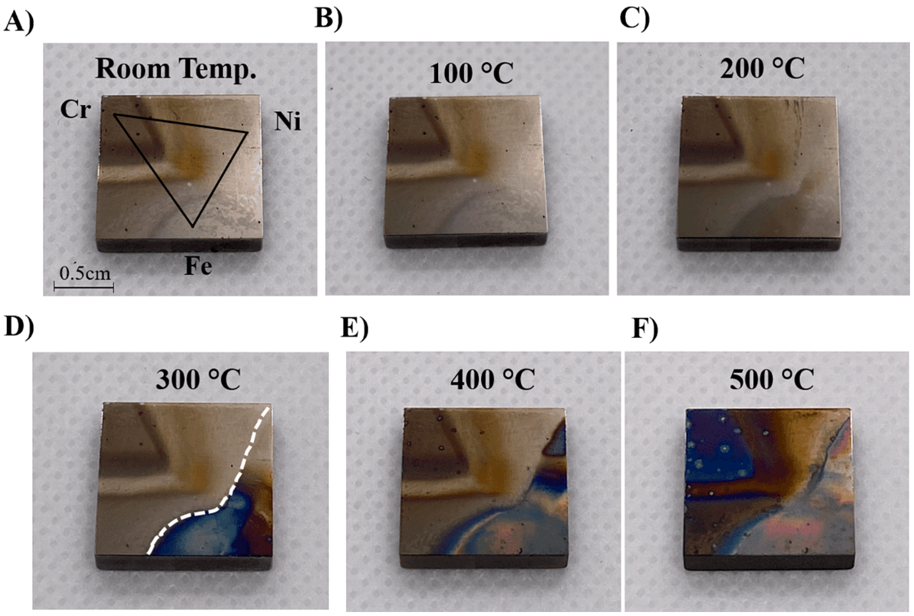

Fig. 2. **A)** Photograph of a $Cr_xFe_yNi_{1-x-y}$ CSAF after deposition. **B)** – **F)** Photographs of the CSAF after sequential oxidation in dry air for 1 h at temperatures from 100 °C → 500 °C. The photo of the CSAF at room temperature is overlaid by a triangle framing the region containing ternary composition space. The vertices are labelled with their corresponding pure components. Fig. 2A shows the film after storage for several weeks at room temperature in ambient air during which no visible changes occurred. This CSAF was deposited with a higher background oxygen pressure than the CSAF in Fig. 1A causing evidence of early surface oxidation. After visually analyzing the progression of oxidative corrosion from 100 °C → 500 °C, 300 °C was chosen as the optimal temperature for further analysis. The sharp boundary (marked by the dashed white line in **D)**) between passivated alloys and alloys showing strong evidence of oxidative corrosion first appears at 300 °C.

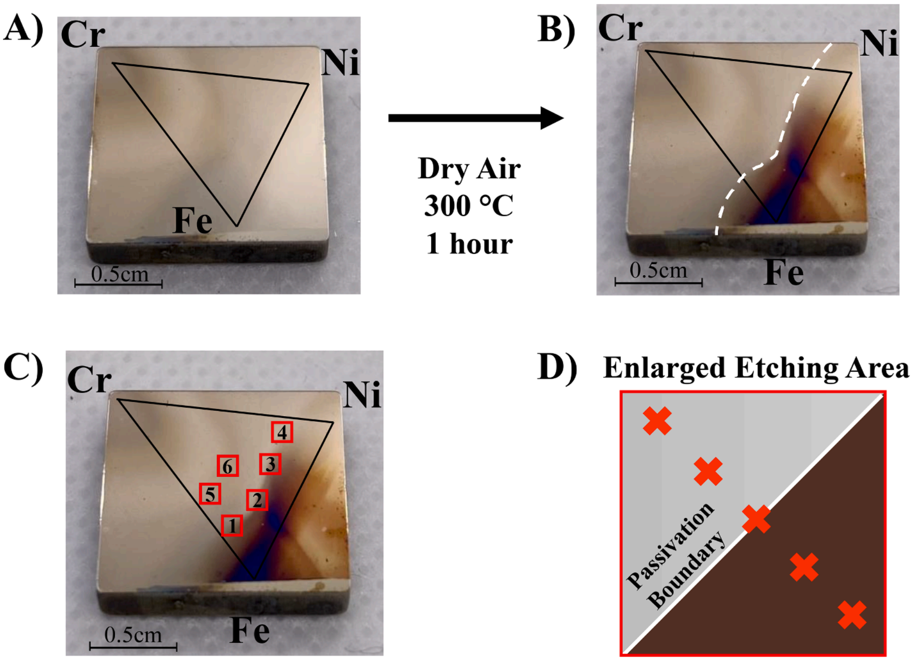

Fig. 3. **A)** Photograph showing the $Cr_xFe_yNi_{1-x-y}$ CSAF from Fig. 1A before oxidation with an overlaid black triangle indicating the region on the CSAF containing ternary composition space with the pure components labelled at the vertices. **B)** Photo of the same CSAF after oxidation in dry air at 300 °C for 1 h. The dashed white line shows the location of the visually observed passivation boundary analogous to the line drawn in Fig. 2D. **C)** The six red squares identifying the areas on the CSAF at which XPS depth profiling was performed after oxidation at 300 °C. The dimensions of the red squares are roughly to scale and show the 1.2×1.2 mm^2 area over which the Ar^+ beam was rastered to excavate the film during depth profiling. **D)** An enlarged view of the etching area framed by each red square shows the 5 analysis points marked by red '×'s where XPS measurements were made. The location of etching areas 1 → 4 were chosen along the visually distinct boundary marked in **B)** separating passivated alloy compositions from those where substantial oxidation was observed. The locations of etching areas 5 and 6 lie in the passivated region of ternary composition space.

strong evidence of oxidative corrosion is displayed in the Fe-rich region and extends into the Fe_xNi_{1-x} binary region. The main difference between Fig. 3B and Fig. 2D is that the extent of oxidative corrosion in the CSAF in Fig. 2 is more advanced since it started in a more oxidized initial state, as already addressed above. Because our aim is to identify a critical Cr composition, x^*_{Cr}, or range of compositions that facilitate the passivation of $Cr_xFe_yNi_{1\text{-}x\text{-}y}$ alloys, the absolute extent of oxidation is not as significant as locating the passivation boundary in composition space. As with the previous sample, the $Cr_xFe_yNi_{1\text{-}x\text{-}y}$ CSAF oxidized at 300 °C has a well-defined passivation boundary that runs nearly parallel to the contours of constant Cr composition (Fig. 1B). This boundary delineates the Fe-rich and $Fe_xNi_{1\text{-}x}$ alloys displaying evidence of oxidative corrosion from Cr-rich alloys displaying evidence of passivation.

After locating the corrosion boundary, specific regions of the CSAF were chosen on which to perform further analysis using XPS depth profiling. The 6 regions at which depth profiling was performed are identified by the red squares in Fig. 3C, four of which lie on the passivation boundary and two of which lie in the Cr-rich passivated region. In order to capture how minor changes in the composition of the ternary alloy result in large changes in the oxidative corrosion resistance, depth profiling was performed over a large enough area such that 5 non-overlapping XPS measurements were obtained across the passivation boundary, as shown in the enlarged etching area in Fig. 3D. At locations 1–6 in Fig. 3C, the Ar^+ gun was rastered over a 1.2×1.2 mm^2 area and five XPS measurements were made at points marked by the red '×'s on the diagonal inside each etched area (Fig. 3D). The Cartesian coordinates of the 30 XPS analysis points were measured using the stage position at each analysis site so that the bulk atomic composition of each alloy could be determined through interpolation of the atomic concentration maps in Fig. 1B, C, and D.

Several calibration experiments were performed before excavation of the $Cr_xFe_yNi_{1\text{-}x\text{-}y}$ CSAF to optimize the ion gun parameters and the depth profiling routine in order to ensure that the datasets obtained accurately reflected the film composition. In particular, we needed to ensure that the Ar^+ etching was performed slowly enough that an adequate number of XPS scans were obtained throughout the depth of the film. When etching is performed too aggressively, too much material is removed between each XPS scan and there is significant information loss in the composition of the film. Optimization of the depth profiling routine is complicated by the fact that the proportion of each element in this ternary alloy system and their relative oxidation state affect the overall etching rate. Furthermore, the effective etching rate likely changes during depth profiling, as the extent of oxidation decreases from the surface to the bulk of the film. The optimal strategy to account for these complications was found to be a three-phase depth profile. First, the top surface layers experiencing large changes in their oxidation states and compositions over a short depth were excavated using 10 measurement cycles each consisting of XPS data collection followed by 10 s of Ar^+ etching. Then, the subsurface was excavated using 18 measurement cycles each consisting of XPS data collection followed by 20 s of Ar^+ etching. Finally, 5 or more measurement cycles consisting of XPS data collection followed by 250 s of Ar^+ etching were used to quickly excavate the bulk and reach the Mo substrate. The accuracy of our three-phase depth profiling routine was confirmed using binary CSAFs for the $Cr_xFe_yNi_{1\text{-}x\text{-}y}$ alloy system. The XPS spectra at each layer of the depth profile was fit (as explained below) to quantify the atomic composition of each element. The atomic composition at each layer of the depth profile was then integrated to yield an average alloy composition at several different analysis locations. Comparing the average alloy compositions obtained by reconstruction of the depth profiles with the bulk alloy compositions determined by interpolation of the EDX measurements showed very small error, with a discrepancy of at most 10 at.% in only a few cases. The agreement of the EDX-derived bulk alloy compositions with the aggregate XPS measurements that reconstructed the excavated alloy layer-by-layer ensures that the depth profiles obtained with our etching parameters capture the true composition of the film with adequate resolution. Despite the fact that etching with the Ar^+ beam is known to be nonuniform [48,51], we ensured that the Mo substrate was reached at all analysis locations by adding extra bulk etching cycles to certain depth profiles when necessary. It is for this reason that we present all depth profiles normalized by the total etching time needed to reach the Mo substrate. The normalized depth of each XPS measurement cycle is defined by dividing the accumulated etching time at the cycle of interest by the total etching time needed to reach the Mo substrate.

As we introduced above in Fig. 3D, each etched area contained five XPS measurement points at which depth profiles through the entire film were constructed. After the XPS measurements were collected, the dataset from each point was treated with CasaXPS processing software to remove the background and fit each alloy component using the following orbitals: Cr $2p_{3/2}$, Fe $2p_{1/2}$, Ni $2p_{3/2}$, and Mo $3d_{5/2}$. The four panels of Fig. 4 illustrate how a depth profile is constructed using XPS spectra collected for the $Cr_{0.22}Ni_{0.78}$ alloy on the oxidized $Cr_xFe_yNi_{1\text{-}x\text{-}y}$ CSAF (Fig. 3B). The depth profile itself showing the XPS-derived at.% composition of each component versus normalized depth is presented in Fig. 4C. The raw XPS spectra (black dots) for Cr *2p* (Fig. 4A) and Ni *2p* (Fig. 4B) collected at a normalized depth ≈ 0.05 (indicated by the dashed black line in Fig. 4C) are shown to demonstrate how the fitting is performed. The Cr $2p_{3/2}$ and Ni $2p_{3/2}$ orbitals in Fig. 4A and B, respectively, were fit by the red curves after deconvoluting the envelopes into their metallic and oxide components. The metallic component of each constituent metal was fit by inserting the reference envelope (light tinted envelopes in Fig. 4A and B) obtained for the pure material and constraining its peak position to lie within the given binding energy range with a $\text{FWHM} = 1 \pm 0.1$. The oxide components (dark tinted envelopes in Fig. 4A and B) were fitted by adding the minimum number of peaks with a fixed 30 % Gaussian/Lorentzian shape to create an envelope that fit the raw spectra with a residual standard deviation ≤ 1.5. The red curves showing the aggregated metallic and oxide envelopes in Fig. 4A and B are overlaid on top of the raw spectra (black dots) to show the goodness of fit.

Once the metallic and oxide proportions comprising each XPS envelope are known, they are scaled using the corresponding Scofield sensitivity factors to obtain the XPS at.% composition, as presented in the composition table in Fig. 4D for normalized depth ≈ 0.05. The bulk at.% composition in Fig. 4D was determined through interpolation of the atomic concentration maps determined by EDX in Fig. 1B → D at the film location where depth profiling was performed. Determination of the XPS-measured at.% composition at all film depths using curve fitting of the collected spectra and scaling with Scofield sensitivity factors resulted in composition tables analogous to Fig. 4D throughout the depth of $Cr_{0.22}Ni_{0.78}$. The $Cr_{0.22}Ni_{0.78}$ depth profile in Fig. 4C is a graphical representation of the calculated XPS at.% composition that combines information gained at each cycle into a single, compact figure. Representing the dataset using such a figure conveys a high volume of information, as the changing composition and extent of oxidation of the alloy can be readily assessed by scanning from the extreme surface at the left to any point in the film depth to the right.

Fig. 5 is analogous to Fig. 4 and shows the construction of a depth profile for the $Cr_{0.31}Fe_{0.69}$ alloy on the oxidized $Cr_xFe_yNi_{1\text{-}x\text{-}y}$ CSAF (Fig. 3B) using the collected XPS spectra. Fig. 5A and 5B show the raw XPS spectra (black dots) for Cr *2p* and Fe *2p*, respectively, collected at a normalized depth ≈ 0.09 (indicated by the black dashed line in Fig. 5C). While the curve fitting of the Cr $2p_{3/2}$ orbital is the same as in Fig. 4A, the Fe $2p_{1/2}$ orbital in Fig. 5B is used to quantify the Fe at.% composition to avoid overlap with the Ni *LMM* Auger transition which occurs in the same binding energy range as Fe $2p_{3/2}$. Following the same procedure as already explained for Fig. 4, curve fitting of the XPS spectra and scaling with Scofield sensitivity factors allowed calculation of the atomic composition table in Fig. 5D. Graphical representation of this quantification of the XPS spectra at every measured film depth is shown in the depth profile for $Cr_{0.31}Fe_{0.69}$ in Fig. 5C. Combined, Figs. 4 and 5 show how the XPS spectra for ternary $Cr_xFe_yNi_{1\text{-}x\text{-}y}$ alloys can be analyzed. By applying the same curve fitting procedure to the Cr $2p_{3/2}$, Fe $2p_{1/2}$, and Ni $2p_{3/2}$ orbitals simultaneously, depth profiles at discrete CSAF locations within ternary composition space can be constructed. Evaluation of these depth profiles at different bulk alloy compositions reveals trends in the oxidative corrosion resistance of the alloy system, and in

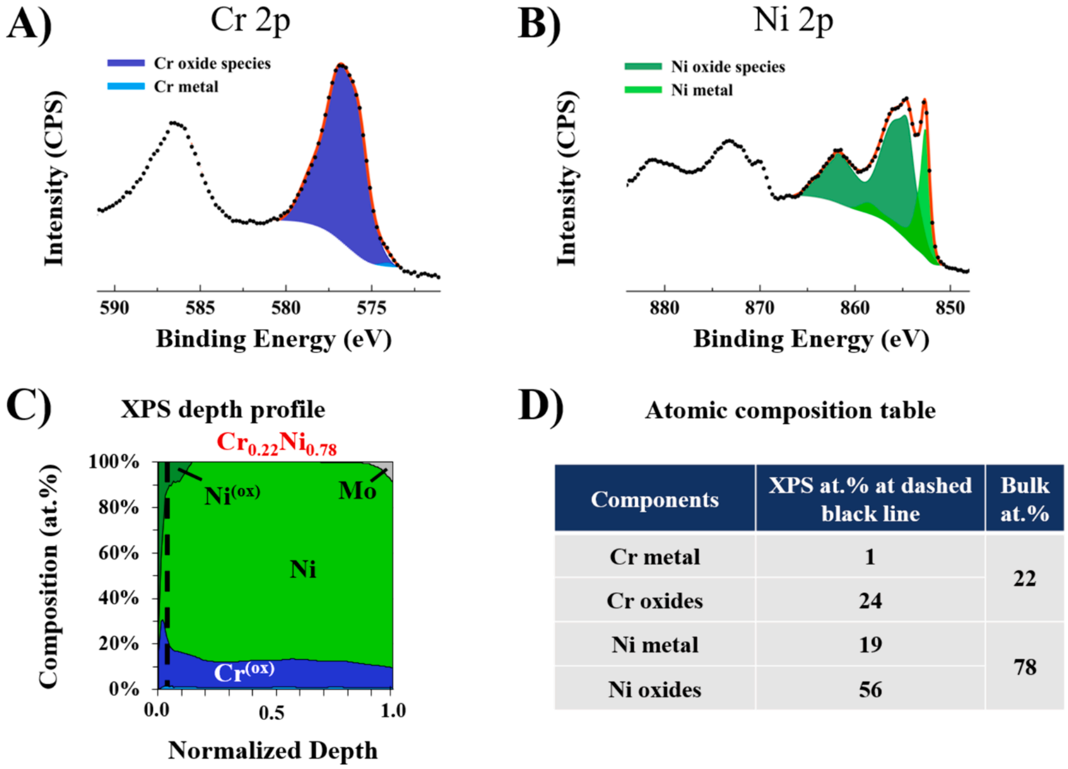

Components	XPS at.% at dashed black line	Bulk at.%
Cr metal	1	22
Cr oxides	24	
Ni metal	19	78
Ni oxides	56	

Fig. 4. **A)** and **B)** Collected Cr *2p* and Ni *2p* XPS spectra (black dots) and their fitted envelopes (red curves) obtained by summing the colored peaks corresponding to the metal and oxide components. The metallic component of the Cr $2p_{3/2}$ and Ni $2p_{3/2}$ spectra were fit using the reference spectra obtained from the pure metals and the oxide components were fit using peaks with a fixed 30 % Gaussian/Lorentzian shape. A minimum number of oxide peaks were added until the fitted envelope reproduced the experimental spectra with a residual standard deviation ≤ 1.5. **C)** Depth profile through the entire thickness of the $Cr_{0.22}Ni_{0.78}$ alloy located inside the Cr_xNi_{1-x} binary region of the oxidized CSAF in Fig. 3B. The depth profile consists of the at.% composition of each component (metallic and oxidized) plotted versus normalized film depth: normalized depth = 0 corresponds to the top surface and normalized depth = 1 corresponds to the appearance of the Mo substrate when the film has been completely removed. Note that normalized depth is found by dividing the etching time at each layer of the depth profile by the total etching time used to completely excavate the film. **D)** Atomic composition table at normalized depth ≈ 0.05 indicated by the dashed black line in **C)** at which point the XPS spectra in **A)** and **B)** were obtained. Scofield sensitivity factors were used to scale the peak areas of the fitted Cr $2p_{3/2}$ and Ni $2p_{3/2}$ spectra in **A)** and **B)** to obtain the XPS at.% compositions. The XPS at.% compositions at each layer of the depth profile were used to construct the depth profile in **C)**. The bulk at.% in **D)** was found through interpolation of the atomic concentration maps (measured by EDX in Fig. 1B → 1D) at the film location where depth profiling was performed.

particular, allows us to identify the critical Cr concentration, x^*_{Cr}.

The utility of creating a layer-by-layer reconstruction of the alloy using depth profiling and XPS curve fitting, as in Figs. 4 and 5, is immediately apparent when considering the breadth of information gleaned about the alloy of interest in a single, compact figure. For example, the depth profiles for $Cr_{0.22}Ni_{0.78}$ and $Cr_{0.31}Fe_{0.69}$ shown in Fig. 4C and Fig. 5C, respectively, show the surface and the bulk of the alloys after oxidation in dry air for 1 h at 300 °C, as well as how the oxidized fraction of each constituent element evolves throughout the depth of the film. The composition tables in Fig. 4D and Fig. 5D show the at.% breakdown of the $Cr_{0.22}Ni_{0.78}$ and $Cr_{0.31}Fe_{0.69}$ alloys near the top surface at the normalized depth indicated by the dashed black lines in Fig. 4C and Fig. 5C. At normalized depth ≈ 0.05 quantified in Fig. 4D, the alloy composition is 24 at.% Cr and 76 at.% Ni, which closely matches the bulk composition of $Cr_{0.22}Ni_{0.78}$ determined by interpolating the atomic concentration maps. The surface is slightly enriched in Cr, which decreases gradually throughout the bulk of the material. As expected, due to the fact that ΔH_f^0 for $Ni^{(ox)}$ is much higher (i.e., less exothermic) than ΔH_f^0 for $Cr^{(ox)}$ (Table 1), $Ni^{(ox)}$ only penetrates to a normalized depth of ~0.15, beyond which Ni only exists in its metallic state. On the other hand, Cr exists almost exclusively as $Cr^{(ox)}$ throughout the entire depth of the film. Comparing the composition tables in Fig. 4D and Fig. 5D reveals that for $Cr_{0.31}Fe_{0.69}$, the surface Cr enrichment ($x_{Cr} = 59$ at.%) is much stronger than for $Cr_{0.22}Ni_{0.78}$ ($x_{Cr} = 25$ at.%). Similar to surface Ni in $Cr_{0.22}Ni_{0.78}$, surface Fe in $Cr_{0.31}Fe_{0.69}$ is nearly completely oxidized, however, in this case, $Fe^{(ox)}$ penetrates through the entire depth of the film.

The depth profiles presented in Fig. 4C and Fig. 5C reveal the oxidative corrosion tendency for two specific binary alloys, $Cr_{0.22}Ni_{0.78}$ and $Cr_{0.31}Fe_{0.69}$, using layer-by-layer reconstructions of the film. The oxides formed in these depth profiles are consistent with thermodynamic expectations for alloy systems containing Cr, Fe, and Ni. In particular, for the $Cr_{0.22}Ni_{0.78}$ binary alloy, Ni is preferentially preserved in its metallic state due to its much less exothermic ΔH_f^0 than Cr. On the other hand, for $Cr_{0.31}Fe_{0.69}$, $Cr^{(ox)}$ and $Fe^{(ox)}$ have comparable enthalpies of formation and, not surprisingly, both are present throughout the bulk of the film. $Cr^{(ox)}$ is also known to form a passivating oxide scale [9–13], and this is observed as surface enrichment of $Cr^{(ox)}$ at low normalized depths in Fig. 5C. On the other hand, Fe becomes mostly metallic for normalized depths ≥ 0.15. Thus, the oxidative corrosion protection provided by Cr is readily apparent from the analysis of both $Cr_{0.22}Ni_{0.78}$ and $Cr_{0.31}Fe_{0.69}$. However, this behavior is expected to depend on the bulk alloy composition and will be further complicated by the addition of a third constituent element within $Cr_xFe_yNi_{1-x-y}$ ternary composition space. For the remainder of the paper, we analyze XPS depth profiles performed at carefully selected locations on the $Cr_xFe_yNi_{1-x-y}$ CSAF based on the visually distinct passivation boundary identified in Fig. 3B. Analysis of these depth profiles allows us to find the critical Cr concentration threshold, x^*_{Cr}, where the resistance to oxidative corrosion changes abruptly with minor changes in the bulk alloy composition.

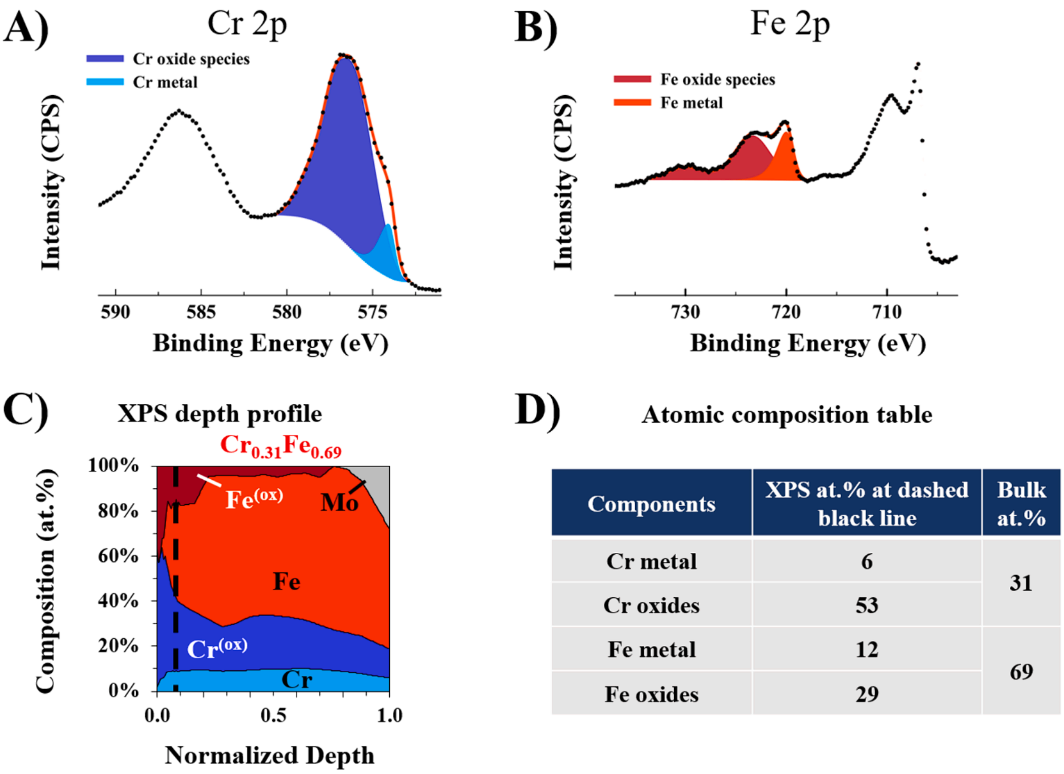

Components	XPS at.% at dashed black line	Bulk at.%
Cr metal	6	31
Cr oxides	53	
Fe metal	12	69
Fe oxides	29	

Fig. 5. **A)** and **B)** Collected Cr *2p* and Fe *2p* XPS spectra (black dots) and their fitted envelopes (red curves) obtained by summing the colored peaks corresponding to the metal and oxide components. The metallic component of the Cr $2p_{3/2}$ and Fe $2p_{1/2}$ spectra were fit using the reference spectra obtained from the pure metals and the oxide components were fit using peaks with a fixed 30 % Gaussian/Lorentzian shape. A minimum number of oxide peaks were added until the fitted envelope reproduced the experimental spectra with a residual standard deviation ≤ 1.5. **C)** Depth profile through the entire film thickness of the $Cr_{0.31}Fe_{0.69}$ alloy located inside the Cr_xFe_{1-x} binary region of the oxidized CSAF in Fig. 3B. The depth profile consists of the at.% composition of each component (metallic and oxidized) plotted versus normalized film depth: normalized depth = 0 corresponds to the top surface and normalized depth = 1 corresponds to the appearance of the Mo substrate when the film has been completely removed. Note that normalized depth is found by dividing the etching time at each layer of the depth profile by the total etching time used to completely excavate the film. **D)** Atomic composition table at normalized depth ≈ 0.09 indicated by the dashed black line in **C)** at which point the XPS spectra in **A)** and **B)** were obtained. Scofield sensitivity factors were used to scale the peak areas of the fitted Cr $2p_{3/2}$ and Fe $2p_{1/2}$ spectra in **A)** and **B)** to obtain the XPS at.% compositions. The XPS at.% compositions at each layer of the depth profile were used to construct the depth profile in **C)**. The bulk at.% in **D)** was found through interpolation of the atomic concentration maps (measured by EDX in Fig. 1B → 1D) at the film location where depth profiling was performed.

3.4. *Determination of x^{*}_{Cr} using XPS depth profiling*

Using the $Cr_xFe_yNi_{1\text{-}x\text{-}y}$ CSAF oxidized for 1 h in dry air at 300 °C, ternary composition space was explored by excavating alloys contained within the 6 etching regions identified in Fig. 3C: regions 1 → 4 lying on the visually observed passivation boundary and regions 5 and 6 lying in the passivated Cr-rich area. During depth profiling, XPS spectra were obtained at 5 points along the diagonal of each etching region (as illustrated in Fig. 3D) resulting in a total of 30 depth profiles within ternary composition space. The 30 depth profiles are presented in Figs. 6 and 7 for etching regions 1, 2, and 3 and regions 4, 5, and 6, respectively, with each row of the figures showing the depth profiles obtained within a single etching region from the upper left corner to the lower right corner. The bulk alloy composition at each point was found using its Cartesian coordinates and interpolating the atomic concentration maps in Fig. 1B, C, and D. The bulk compositions corresponding to each analysis location are shown above the depth profiles in Figs. 6 and 7. Thus, by scanning a particular row in Figs. 6 and 7 from left to right, one can readily appreciate how small changes in the bulk composition of the alloy lead to significant changes in the oxidative corrosion resistance based upon the evolution of the depth profiles. It is worthwhile to note that due to the orientation at which the CSAF composition gradients were deposited and the angle of the line scan, each etching region is nearly constant in Fe composition, while the Cr composition decreases, and the Ni composition increases from left to right. In other words, the bulk value of x_{Fe} changes minimally within each row of Figs. 6 and 7 to isolate how changes in Cr and Ni content affect the resistance to oxidative corrosion within composition space. This choice was intentional since Cr is known to form a passivating oxide layer [9–13] and Ni possesses the lowest inherent oxidation potential of the ternary alloy system.

The protection against oxidative corrosion offered by Cr is readily apparent when examining the most Cr-rich alloy in each etching region in the leftmost column of Figs. 6 and 7 (i.e., Fig. 6A, F, K, Fig. 7A, F, and K). Scanning down this column, it is clear that Cr readily segregates to the surface and oxidizes to $Cr^{(ox)}$ in $Cr_xFe_yNi_{1\text{-}x\text{-}y}$ ternary alloys. Even with as little as $x_{Cr} = 24$–25 at.%, as in Fig. 6F and 6 K, the depth profile reveals the growth of a thick passivation layer of $Cr^{(ox)}$ that completely protects Ni and Fe from oxidative corrosion. In cases where the bulk composition of one of the other components is sufficiently high (i.e., ≥ 65 – 68 at.%), as in Fig. 6A and Fig. 7A, $Cr^{(ox)}$ covers most of the top surface and provides some protection against oxidative corrosion, but does not completely prevent it. When the component present in excess is Fe (top row of Fig. 6), Fe on the top surface is completely oxidized and this $Fe^{(ox)}$ penetrates to a normalized depth of ∼ 0.25 even with $x_{Cr} = 31$ at.% (Fig. 6A). As the bulk Cr composition decreases across the top row of Fig. 6, $Fe^{(ox)}$ composes a higher and higher percentage of the top surface and penetrates deeper and deeper into the film until it reaches bulk oxidation at 23 at.% Cr in Fig. 6D. On the other hand, when Ni is present in excess (top row of Fig. 7), most of the Ni remains in its metallic state due to its inherently high resistance to oxidative corrosion. In fact, as the bulk Cr composition decreases in the Ni-rich alloys across

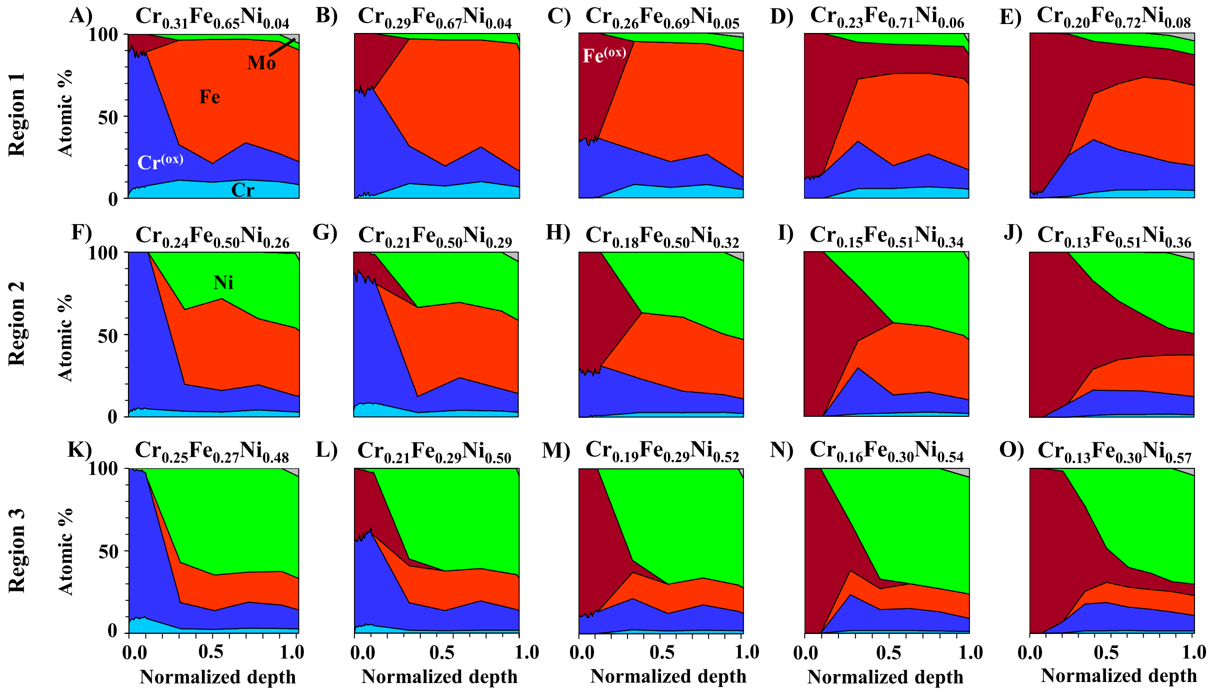

Fig. 6. XPS depth profiles across the passivation boundary for regions 1 (top row), 2 (middle row), and 3 (bottom row) framed by the numbered red etching areas in Fig. 3C. Film components are labelled as follows: Cr = light blue, $Cr^{(ox)}$ = dark blue, Fe = red, $Fe^{(ox)}$ = maroon, Ni = green, $Ni^{(ox)}$ = dark green, Mo = gray. The first figure in each row corresponds to the XPS analysis site in the upper left corner of the etching area in Fig. 3D and each subsequent figure in the row corresponds to the next point in the line scan. The exact coordinates of each XPS measurement were used to interpolate the EDX composition maps in Fig. 1B, 1C, and 1D to give the bulk composition of the alloy above each depth profile. On the passivated side of each etched region there is a layer of $Cr^{(ox)}$ at the extreme surface that prevents the bulk oxidation of either Fe or Ni. Small decreases in the bulk Cr composition along each row lead to the bulk oxidation of Fe, while Ni remains metallic due to its higher intrinsic oxidative corrosion resistance.

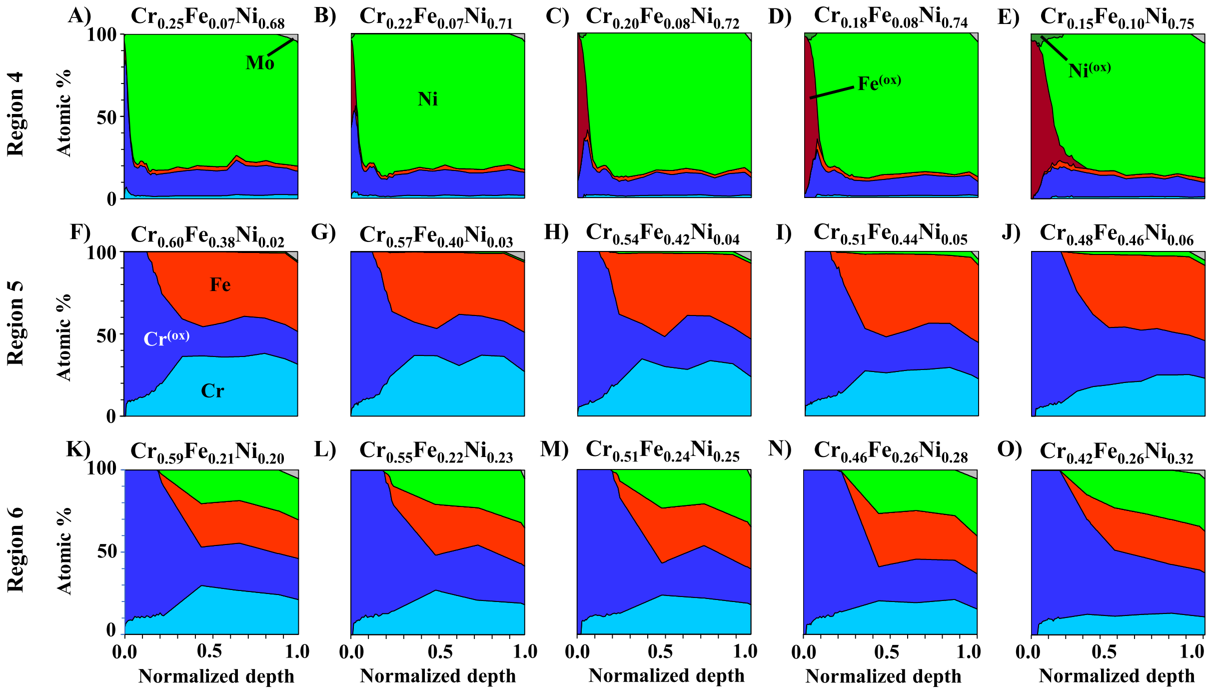

Fig. 7. XPS depth profiles across the passivation boundary for regions 4 (top row), 5 (middle row), and 6 (bottom row) framed by the numbered red etching areas in Fig. 3C. Film components are labelled as follows: Cr = light blue, $Cr^{(ox)}$ = dark blue, Fe = red, $Fe^{(ox)}$ = maroon, Ni = green, $Ni^{(ox)}$ = dark green, Mo = gray. The first figure in each row corresponds to the XPS analysis site in the upper left corner of the etching area in Fig. 3D and each subsequent figure in the row corresponds to the next point in the line scan. The exact coordinates of each XPS measurement were used to interpolate the EDX composition gradients in Fig. 1B, 1C, and 1D to give the bulk composition of the alloy above each depth profile. Region 4 shows that the oxidation of Fe is passivated only when the bulk composition of Cr is $\geq$ 22 at.%, below which the Fe is drawn to the surface and completely oxidized. Cr-rich regions 5 and 6 show complete oxidative corrosion protection due to the formation of a sufficiently thick $Cr^{(ox)}$ passivation layer.

the top row of Fig. 7, the small quantity of Fe present in the material (~7–9 at.%) is drawn to the top surface and oxidized to replace the depleted Cr, leaving the Ni in the bulk almost completely preserved.

When no alloy component is present in excess, the amount of bulk Cr needed to prevent oxidative corrosion is greatly reduced, as shown by the thick passivation layers formed in Fig. 6F and 6 K at $x_{Cr} = 24$ at.% that completely protect the Fe and Ni present underneath. As the bulk Cr content decreases across the middle and bottom rows of Fig. 6, x_{Cr} falls below the amount necessary to maintain a passivation layer and is gradually replaced by $Fe^{(ox)}$, while Ni stays in the bulk and remains metallic. When x_{Cr} is decreased to 15–16 at.%, as in Fig. 6I and 6 N, $Fe^{(ox)}$ eventually composes 100 % of the top surface and penetrates to a normalized depth of ~ 0.5. Decreasing x_{Cr} slightly further to 13 at.% leads to significant $Fe^{(ox)}$ penetration through the bulk of the material, as in Fig. 6J and 6O. The remarkably different oxidative corrosion resistance observed when x_{Cr} is changed from 25 at.% → 13 at.% in the middle and bottom rows of Fig. 6 shows, with high reproducibility, the extreme sensitivity of alloy properties to their bulk composition, and in particular, x_{Cr}.

The oxidative corrosion resistance of $Cr_xFe_yNi_{1-x-y}$ alloys is most sensitive to alloy composition around the critical Cr composition, x^*_{Cr}, above which a passivating $Cr^{(ox)}$ layer completely prevents the oxidation of the other constituent metals. When $x_{Cr} \geq x^*_{Cr}$, the alloy components are preserved and experience no oxidation underneath the $Cr^{(ox)}$ passivation layer. This behavior is clearly observed in the middle and bottom rows of Fig. 7, where x_{Cr} ranges from 60 to 42 at.%. Within these two etched regions, the depth profiles are nearly identical, with $Cr^{(ox)}$ passivation layers of similar thicknesses covering the extreme surface and Fe and Ni being 100 % metallic throughout the bulk. As x_{Cr} decreases within this range, the $Cr^{(ox)}$ layer is maintained while the amount of metallic Cr present in the bulk steadily decreases. Thus, for alloys with $x_{Cr} \geq x^*_{Cr}$, (i.e., Fig. 7F → O, Fig. 6F, and K) the depth profile reflects the bulk alloy composition interpolated from the EDX maps capped by a passivating layer of $Cr^{(ox)}$ that penetrates through the entire film. Conversely, when $x_{Cr} < x^*_{Cr}$, (i.e., Fig. 6A → E, Fig. 6G → J, Fig. 6L → O, and Fig. 7A → E) the Cr content is too low to form a uniform $Cr^{(ox)}$ passivation layer of sufficient thickness to prevent the oxidative corrosion of Fe and/or Ni.

Determination of the exact location of x^*_{Cr} within $Cr_xFe_yNi_{1-x-y}$ composition space is complicated by the fact that the overall bulk composition of the alloy affects the amount of Cr required to form the $Cr^{(ox)}$ passivation layer. For example, $x^*_{Cr} \approx 24$–25 at.% from the depth profiles for $Cr_{0.24}Fe_{0.50}Ni_{0.26}$ and $Cr_{0.25}Fe_{0.27}Ni_{0.48}$ in Fig. 6F and K, respectively. However, when excess Fe is present, as in Fig. 6C, $x^*_{Cr} > 26$ at.% due to the incomplete passivation of $Cr_{0.26}Fe_{0.69}Ni_{0.05}$. Since performing depth profiling across all of ternary composition space is impractical, we can use the passivation boundary identified visually in Fig. 3B as our guide for mapping the trajectory of x^*_{Cr} within composition space. The depth profiles performed within the 4 etching regions along this visually observed passivation boundary in Figs. 6 and 7 confirm that the midpoint of each line scan, lying right on the boundary itself, is the point at which $Cr^{(ox)}$ on the top surface falls below 50 % and is replaced by either $Fe^{(ox)}$ or a mixture of $Fe^{(ox)}$ and $Ni^{(ox)}$, as in Fig. 6C, H, M, and Fig. 7C. In other words, the passivation boundary identified visually in Fig. 3B corresponds to the location where the passivating $Cr^{(ox)}$ layer no longer composes the majority of the top surface, and we adopt this definition for x^*_{Cr} to map its trajectory through $Cr_xFe_yNi_{1-x-y}$ composition space.

4. Discussion

The depth profiles analyzed in Figs. 6 and 7 revealed that the midpoint of the line scan within each etched area along the visually observed passivation boundary approximated the Cr bulk composition where $Cr^{(ox)}$ failed to cover at least 50 % of the topmost surface leading to the appearance of $Fe^{(ox)}$ and/or $Ni^{(ox)}$ on the surface and penetrating into the bulk. The location of these points right along the visually distinct passivation boundary indicates that the critical Cr composition threshold, x^*_{Cr}, can be defined by the dashed white line identified in Fig. 3B since it marks the location where bulk oxidative corrosion begins, as confirmed in the XPS depth profiles. Consequently, the coordinates of the dashed white line in Fig. 3B can be used to interpolate the EDX measurements of bulk alloy composition in Fig. 1B, 1C, and 1D to plot the trajectory of x^*_{Cr} within $Cr_xFe_yNi_{1-x-y}$ composition space. The red curve in Fig. 8 shows the trajectory of x^*_{Cr} within ternary composition space obtained by transforming the real-space boundary identified in Fig. 3B into a bulk alloy composition boundary. The four black '×'s in Fig. 8 correspond to the bulk alloy compositions in Fig. 6C, 6H, 6 M, and 7C which lie at the midpoint of the line scan within the etched areas along the passivation boundary. Note that these bulk compositions lie on or slightly to the left of x^*_{Cr} because they indicate either the onset of oxidative corrosion or a point at which significant bulk oxidation has already occurred.

Interestingly, Fig. 8 shows that x^*_{Cr} reaches its minimum value of ~ 18 at.% with nearly equimolar amounts of Fe and Ni at $Cr_{0.18}Fe_{0.40}Ni_{0.42}$. Increasing the proportion of either Fe or Ni leads to an increase in x^*_{Cr} to as much as ~ 26 at.% for Cr_xFe_{1-x} and to ~ 20 at.% for Cr_xNi_{1-x}, but overall, the trajectory of x^*_{Cr} adheres fairly strictly to the contours of constant Cr composition shown in Fig. 1B. This confirms that Cr content is the most important factor for determining a $Cr_xFe_yNi_{1-x-y}$ alloy's resistance to oxidative corrosion. In other words, all alloys to the right of the boundary demarcated by x^*_{Cr} will achieve comparable levels of oxidative corrosion protection independent of whether the material is composed mostly of Fe or Ni. As Fe → 0 %, x^*_{Cr} decreases slightly from ~23 at.% for Ni-rich ternary alloys to ~20 at.% for binary Cr_xNi_{1-x}

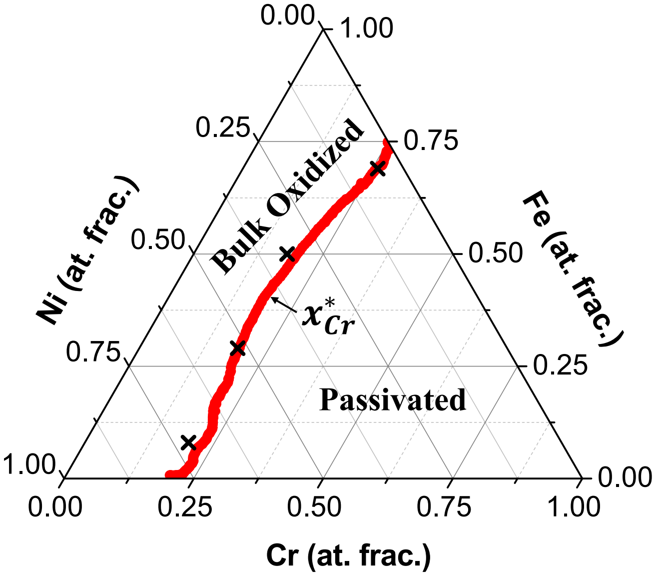

Fig. 8. Trajectory (red curve) of x^*_{Cr} plotted within $Cr_xFe_yNi_{1-x-y}$ ternary composition space using the coordinates of the visually observed passivation boundary in Fig. 3B. The four black '×'s correspond to the bulk alloy compositions in Fig. 6C, 6H, 6 M, and 7C at which $Cr^{(ox)}$ no longer forms a passivating layer, leading to the appearance of at least 50 % $Fe^{(ox)}$ and/or $Ni^{(ox)}$ on the top surface. These XPS depth profiled compositions lie n or slightly to the left of the red curve tracing x^*_{Cr} because they indicate either the onset of oxidative corrosion or a point at which significant bulk oxidation has already occurred. The value of x^*_{Cr} reaches its minimum value of ~ 18 at.% at nearly equimolar Fe and Ni concentrations, $Cr_{0.18}Fe_{0.40}Ni_{0.42}$, and increases as the proportion of either component is increased. For Cr_xFe_{1-x} binary alloys, x^*_{Cr} increases to ~ 26 at.%, while for Cr_xNi_{1-x} binary alloys, x^*_{Cr} only increases to ~ 20 at.%, reflecting the naturally lower oxidation potential of Ni compared to Fe.

alloys. The critical Cr composition needed to passivate Cr_xNi_{1-x} alloys is lower than for Cr_xFe_{1-x} alloys which reflects the inherently lower oxidation potential of Ni relative to Fe due to its less exothermic ΔH_f^0 (Table 1). However, since x_{Cr}^* reaches its minimum within ternary composition space, the alloying of Cr, Fe, and Ni offers greater resistance to oxidative corrosion than its constituent elements and offers a broad composition range over which the bulk alloy composition can be tuned for the optimization of another material property. Ultimately, mapping x_{Cr}^* in this way aids in the design of new materials by identifying the threshold of bulk Cr composition where adequate protection against oxidative corrosion is no longer achieved.

For reference, an equilibrium phase diagram for the $Cr_xFe_yNi_{1-x-y}$ alloy system at 650 °C [52] can be found in Figure S2 of the Supporting Information. In $Cr_xFe_yNi_{1-x-y}$ composition space, there are three possible crystal structures depending on the bulk alloy composition: an austenitic face centered cubic (FCC) structure, a Fe-rich body centered cubic (BCC) structure, and a Cr-rich BCC structure. The superposition of x_{Cr}^* from Fig. 8 onto the phase diagram in Figure S2 shows that it does not fall along any phase boundaries, but traverses 4 different phases within composition space. Thus, the bulk alloy composition seems to be the dominant factor in determining the resistance to oxidative corrosion, and not the crystal structure.

At this point, we can summarize some of the general trends observed from analysis of the oxidative corrosion tendencies of this ternary alloy system and compare them with expectations obtained from literature. First, we note that only Cr can form a passivating oxide layer [9–13], while Fe and Ni cannot. When Fe segregates to the surface and oxidizes, as in Fig. 7C, D, and E, the $Fe^{(ox)}$ layer present on the top surface does not prevent the subsurface oxidation of Cr and Ni, and $Cr^{(ox)}$ is even present throughout the bulk of the material. Thus, despite being readily oxidized, $Fe^{(ox)}$ does not stop oxygen from interacting with other components deeper in the film the way that $Cr^{(ox)}$ is able to halt Fe and Ni oxidation in Fig. 7A and 7B. By contrast, Ni is never preferentially surface segregated in Figs. 6 and 7, as it has the lowest tendency to be oxidized and leaves the other components vulnerable. Therefore, only Cr is capable of forming a passivation layer and does so when a continuous $Cr^{(ox)}$ layer is thick enough to protect the alloy components underneath. This passivation layer can vary in thickness from a few to tens of nm depending on the amount of Cr present in the bulk.

The trends noted above are consistent with thermodynamic expectations when comparing the values of ΔH_f^0 in Table 1 for all of the relevant oxides in this alloy system. Note that the formation of hydroxides and carbides is assumed to be negligible and was excluded from consideration since the oxidation occurred in dry air (i.e., O_2 in N_2), meaning that there was no source of either hydrogen or carbon. The relevant standard enthalpies of oxide formation from Table 1 are $\Delta H_f^0 =$ -239.7 kJ/mol for NiO, $\Delta H_f^0 =$ -1118.4 kJ/mol for Fe_3O_4, and $\Delta H_f^0 =$ -1139.7 kJ/mol for Cr_2O_3 since they are the most thermodynamically favorable oxides to exist in this system without further surface characterization [19–22]. The lowest (i.e., the most exothermic) ΔH_f^0 belongs to Cr_2O_3, which is, therefore, expected to be the most stable. Since the ΔH_f^0 for Fe_3O_4 is comparable to that of Cr_2O_3, some $Fe^{(ox)}$ is expected to form in competition with $Cr^{(ox)}$. In contrast, the ΔH_f^0 for NiO is greater than Cr_2O_3 and Fe_3O_4 by an order of magnitude leading to minimal $Ni^{(ox)}$ formation in systems also containing Cr and/or Fe. These expectations derived from thermodynamic quantities are consistent with the results presented in Figs. 6 and 7 and provide an energetic rationale for the formation of the $Cr^{(ox)}$ passivating layer in alloys where $x_{Cr} \geq x_{Cr}^*$.

The results obtained using our $Cr_xFe_yNi_{1-x-y}$ CSAF are also consistent with the oxidation behavior for other alloy systems. For example, the resistance to oxidative corrosion in dry air has already been studied using a $Al_xFe_yNi_{1-x-y}$ CSAF similar to the one used in this work at slightly harsher oxidation conditions [34]. After oxidation in dry air for 1 h at 427 °C (compared to 300 °C used here), Payne *et al.* were able to identify several distinct regions of the CSAF with different oxidation behavior and plot the trajectory of the critical aluminum concentration, x_{Al}^*, through $Al_xFe_yNi_{1-x-y}$ composition space since $Al^{(ox)}$ forms a passivation layer similar to $Cr^{(ox)}$ [34]. The values of x_{Al}^* were found to range between 15–29 at.%, which are comparable, although span a larger range than the values of x_{Cr}^* found in this work, which lie between 18–26 at.%. Thus, switching one passivating agent, Al, for another, Cr, in a ternary system containing Fe and Ni seems, at first glance, not to result in much change. However, interestingly, in the $Al_xFe_yNi_{1-x-y}$ system, x_{Al}^* for Al_xFe_{1-x} binary alloys is less than x_{Al}^* for Al_xNi_{1-x} binary alloys, which is surprising given the inherently low oxidation potential of Ni. By contrast, within $Cr_xFe_yNi_{1-x-y}$ composition space, x_{Cr}^* for Cr_xFe_{1-x} binary alloys ($x_{Cr}^* \approx 26$ at.%) is nearly 30 % higher than x_{Cr}^* for Cr_xNi_{1-x} binary alloys ($x_{Cr}^* \approx 20$ at.%), which is more consistent with thermodynamic expectations. In addition, the minimum value of x_{Cr}^* within composition space lies at $Cr_{0.18}Fe_{0.40}Ni_{0.42}$, whereas the minimum value for x_{Al}^*, $Al_{0.15}Fe_{0.74}Ni_{0.11}$, has a much higher amount of Fe relative to Ni. While a more direct comparison would have been possible at the same oxidation temperature, these differences between $Cr_xFe_yNi_{1-x-y}$ and $Al_xFe_yNi_{1-x-y}$ highlight the complex interactions between the constituent metals and the oxidizing environment that affect an alloy's functional properties. Nonetheless, the results obtained on these ternary CSAFs are comparable and complementary in their characterization of oxidative corrosion resistance within high-dimensional alloy composition space.

It is worth noting that the range of x_{Cr}^* between 18–26 at.% found within $Cr_xFe_yNi_{1-x-y}$ composition space is consistent with the composition of most corrosion-resistant stainless steels, which consist predominantly of Cr, Fe, and Ni and sometimes contain trace amounts of other elements, like Mo, N, or Cu. For example, commercially relevant stainless steels 304L and 316L, which are used in numerous industrial processes and consumer products, contain $x_{Cr} = 18.5$ at.% and $x_{Cr} = 17.5$ at.%, respectively [53]. The Cr content of these austenitic stainless steels is at the lower limit of x_{Cr}^* found in this study, and this might explain why grades 304L and 316L are only suitable for use in low to mildly corrosive environments [53]. In fact, stainless steel grades 304L and 316L with relatively low Cr content are now starting to be replaced by so-called duplex and "superduplex" grade stainless steels in industrial processes like desalination and in chemical tankers [53]. These duplex grades of stainless steel possess notably higher Cr content, $x_{Cr} = 22.5$–25 at.%, than their austenitic predecessors and this likely explains their increased durability in harsh corrosive environments [53]. Thus, the trajectory of x_{Cr}^* plotted within $Cr_xFe_yNi_{1-x-y}$ composition space corroborates the trend toward using stainless steel grades with a higher proportion of Cr and shows how understanding the oxidative corrosion resistance as a function of the bulk alloy composition can assist in the rapid development of new materials.

5. Conclusions

The resistance to oxidative corrosion of a ternary $Cr_xFe_yNi_{1-x-y}$ CSAF was studied using XPS and Ar^+ depth profiling and was linked to the bulk composition of the alloy derived from EDX measurements. Oxidation was performed in dry air for 1 h at temperatures between 100 – 500 °C before ultimately choosing 300 °C for further analysis. At 300 °C, a visual passivation boundary first appeared sharply dividing $Cr_xFe_yNi_{1-x-y}$ alloys with evidence of advanced bulk oxidation from those that were preserved by a passivating $Cr^{(ox)}$ layer. The visual passivation boundary ran nearly parallel to the contours of constant Cr composition on the CSAF, highlighting the important corrosion-resistant properties of Cr within this alloy system. XPS depth profiling was performed on both sides of the visual passivation boundary to determine how changes in the bulk alloy composition affected the composition of the oxide layer and its penetration depth into the film, leading to the determination of a critical Cr composition threshold, x_{Cr}^{*}. As expected, alloys having $x_{Cr} \geq x_{Cr}^{*}$ had a sufficiently thick layer of passivating $Cr^{(ox)}$ covering the topmost surface that completely protected Fe and Ni from undergoing any oxidation. On the other hand, when $x_{Cr} < x_{Cr}^{*}$, significant amounts of $Fe^{(ox)}$ and/or $Ni^{(ox)}$ were measured on the surface and, in some cases, extended through the bulk of the film, which are indicators of bulk oxidative corrosion. XPS depth profiling confirmed that the visually observed passivation boundary on the CSAF corresponded to the location of x_{Cr}^{*} at which the onset of oxidative corrosion first occurs. Plotting the trajectory of x_{Cr}^{*} within $Cr_xFe_yNi_{1-x-y}$ composition space showed that x_{Cr}^{*} ranged between 18–26 at.% and reaches its minimum at $Cr_{0.18}Fe_{0.40}Ni_{0.42}$. We also observed that x_{Cr}^{*} for Cr_xNi_{1-x} binary alloys is less than x_{Cr}^{*} for Cr_xFe_{1-x} binary alloys, which is consistent with the inherently lower oxidation tendency of Ni relative to Fe. The values of x_{Cr}^{*} found in this work lie within the range of x_{Al}^{*} found for a similar $Al_xFe_yNi_{1-x-y}$ alloy system and correspond to the current grades of commercially available stainless steel used in numerous industrial applications.

CRediT authorship contribution statement

Camille Ferris: Writing – review & editing, Writing – original draft, Visualization, Validation, Formal analysis, Data curation. **Nicholas Golio:** Writing – review & editing, Writing – original draft, Visualization, Validation, Formal analysis, Data curation. **Hervé Martinez:** Writing – review & editing, Project administration. **Andrew J. Gellman:** Writing – review & editing, Supervision, Project administration, Funding acquisition.

Declaration of competing interest

The authors declare that they have no known competing financial interests or personal relationships that could have appeared to influence the work reported in this paper.

Data availability

Data will be made available on request.

Acknowledgements

The authors would like to acknowledge financial support for this work from the International Chair program of the E2S Project funded by the University of Pau and the Adour Countries (UPPA).

Appendix A. Supplementary material

Supplementary material to this article can be found online at https://doi.org/10.1016/j.apsusc.2024.160391.

References

[1] W.C.H.C.T. SIMS, The Superalloys, John Wiley and Sons, New York, 1972.
[2] G. Prashar, H. Vasudev, Hot corrosion behavior of super alloys, Mater. Today Proc. 26 (2019) 1131–1135, https://doi.org/10.1016/j.matpr.2020.02.226.
[3] P. Heritier, Superalliages, Techniques de l'Ingénieur M4770V1 (2022). doi: 10.51257/a-v1-m4770.
[4] C. Rae, Alloys by design: modelling next generation superalloys, Mater. Sci. Technol. 25 (2009) 479–487, https://doi.org/10.1179/174328408X372056.
[5] F.S. Pettit, G.H. Meier, Oxidation and Hot Corrosion of Superalloys, in: Superalloys 1984 (Fifth International Symposium), TMS, 1984: pp. 651–687. doi: 10.7449/1984/Superalloys_1984_651_687.
[6] B.A. Pint, J.R. DiStefano, I.G. Wright, Oxidation resistance: one barrier to moving beyond Ni-base superalloys, Mater. Sci. Eng. A 415 (2006) 255–263, https://doi.org/10.1016/J.MSEA.2005.09.091.
[7] M.P. Brady, I.G. Wright, B. Gleeson, Alloy design strategies for promoting protective oxide-scale formation, JOM 52 (2000) 16–21, https://doi.org/10.1007/s11837-000-0109-x.
[8] F.H. Stott, G.C. Wood, J. Stringer, The influence of alloying elements on the development and maintenance of protective scales, Oxid. Met. 44 (1995) 113–145, https://doi.org/10.1007/BF01046725.
[9] Y. Shi, B. Yang, P.K. Liaw, Corrosion-resistant high-entropy alloys: a review, Metals (Basel) 7 (2017) 1–18, https://doi.org/10.3390/met7020043.
[10] Y. Qiu, S. Thomas, M.A. Gibson, H.L. Fraser, N. Birbilis, Corrosion of high entropy alloys, Npj Mater. Degrad 1 (2017) 1–17, https://doi.org/10.1038/s41529-017-0009-y.
[11] D. König, C. Eberling, M. Kieschnick, S. Virtanen, A. Ludwig, High-throughput investigation of the oxidation and phase constitution of thin-film Ni-Al-Cr materials libraries, Adv. Eng. Mater. 17 (2015) 1365–1373, https://doi.org/10.1002/adem.201500023.
[12] C. Tang, H. Shi, A. Jianu, A. Weisenburger, G. Victor, M. Grosse, G. Müller, H. J. Seifert, M. Steinbrück, High-temperature oxidation of AlCrFeNi-(Mn or Co) high-entropy alloys: Effect of atmosphere and reactive element addition, Corros. Sci. 192 (2021) 109809, https://doi.org/10.1016/j.corsci.2021.109809.
[13] M. Zhang, X. Shi, Z. Li, H. Xu, G. Li, Corrosion behaviors and mechanism of $CrFeNi_2$ based high-entropy alloys, Corros. Sci. 207 (2022) 110562, https://doi.org/10.1016/j.corsci.2022.110562.
[14] S. Kamal, R. Jayaganthan, S. Prakash, S. Kumar, Hot corrosion behavior of detonation gun sprayed Cr_3C_2-NiCr coatings on Ni and Fe-based superalloys in Na_2SO_4-60% V_2O_5 environment at 900 °C, J. Alloys Compd. 463 (2008) 358–372, https://doi.org/10.1016/j.jallcom.2007.09.019.
[15] P. Dolle, M. Alnot, J.J. Ehrhardt, A. Cassuto, Etude par spectroscopie de photoelectrons et d'electrons auger des etapes initiales de l'oxydation du chrome polycristallin, J. Electron. Spectros. Relat Phenomena 17 (1979) 299–321.
[16] B. Stypula, J. Stoch, The characterization of passive films on chromium electrodes by XPS, Corros. Sci. 36 (1994) 2159–2167, https://doi.org/10.1016/0010-938X(94)90014-0.
[17] P.F. King, H.H. Uhlig, Passivity in the iron-chromium binary alloys, J. Phys. Chem. 63 (1959) 2026–2032, https://doi.org/10.1021/j150582a012.
[18] C. Wagner, Theoretical analysis of the diffusion processes determining the oxidation rate of alloys, J. Electrochem. Soc. 99 (1952) 369, https://doi.org/10.1149/1.2779605.
[19] J.J. Reed, Digitizing the nbs tables of chemical thermodynamic properties: selected values for inorganic and C1 and C2 organic substances in SI units, J. Res. Natl. Inst. Stand. Technol. 125 (2020).
[20] D.R. Lide, CRC handbook of chemistry and physics, CRC Press, 2004.
[21] B.J. Boyle, E.G. King, K.C. Conway, Heats of formation of nickel and cobalt oxides (NiO and CoO) of combustion calorimetry, J. Am. Chem. Soc. 76 (1954) 3835–3837, https://doi.org/10.1021/ja01643a072.
[22] P. Pradyot, Handbook of Inorganic, (2003).
[23] M.P. Brady, Y. Yamamoto, M.L. Santella, P.J. Maziasz, B.A. Pint, C.T. Liu, Z.P. Lu, H. Bei, The development of alumina-forming austenitic stainless steels for high-temperature structural use, JOM 60 (2008) 12–18, https://doi.org/10.1007/s11837-008-0083-2.
[24] Y. Yamamoto, M.P. Brady, M.L. Santella, H. Bei, P.J. Maziasz, B.A. Pint, Overview of strategies for high-temperature creep and oxidation resistance of alumina-forming austenitic stainless steels, Metall. Mater. Trans. A Phys. Metall. Mater. Sci. 42 (2011) 922–931, https://doi.org/10.1007/s11661-010-0295-2.
[25] M.P. Brady, Y. Yamamoto, M.L. Santella, L.R. Walker, Composition, microstructure, and water vapor effects on internal/external oxidation of alumina-forming austenitic stainless steels, Oxid. Met. 72 (2009) 311–333, https://doi.org/10.1007/s11085-009-9161-2.
[26] J. Huang, H. Fang, X. Fu, F. Huang, H. Wan, Q. Zhang, S. Deng, J. Zu, High-temperature oxidation behavior and mechanism of a new type of wrought Ni-Fe-Cr-Al superalloy up to 1300 °C, Oxid. Met. 53 (2000) 273–287, https://doi.org/10.1023/a:1004537119922.
[27] C. Jason Metting, J. Kenneth Bunn, E. Underwood, S. Smoak, J. Hattrick-Simpers, Combinatorial approach to turbine bond coat discovery, ACS Comb. Sci. 15 (2013) 419–424, https://doi.org/10.1021/co3000902.
[28] T. Gebhardt, D. Music, T. Takahashi, J.M. Schneider, Combinatorial thin film materials science: from alloy discovery and optimization to alloy design, Thin Solid Films 520 (2012) 5491–5499, https://doi.org/10.1016/J.TSF.2012.04.062.
[29] A. Hagemeyer, P. Strasser, A.F. Volpe, High-Throughput Screening in Chemical Catalysis, WILEY-VCH, Weinheim, 2004.
[30] J.B. Gerken, J.Y.C. Chen, R.C. Massé, A.B. Powell, S.S. Stahl, Development of an O_2-sensitive fluorescence-quenching assay for the combinatorial discovery of electrocatalysts for water oxidation, Angew. Chemie – Int. Ed. 51 (2012) 6676–6680, https://doi.org/10.1002/anie.201201999.
[31] N. Golio, I. Sen, Z. Guo, R. Railkar, A.J. Gellman, Kinetic parameter estimation for catalytic H_2–D_2 exchange on Pd, Catal. Lett. (2022), https://doi.org/10.1007/S10562-022-03961-0.
[32] N. Golio, A.J. Gellman, Activation by O_2 of Ag_xPd_{1-x} Alloy catalysts for ethylene hydrogenation, ACS Catal. 13 (2023) 14548–14561, https://doi.org/10.1021/acscatal.3c03253.
[33] C. Ferris, N. Golio, H. Martinez, A.J. Gellman, Alloy corrosion and passivation spanning composition space, Chem. Commun. 59 (2023) 8660–8675, https://doi.org/10.1039/d3cc01852k.
[34] M.A. Payne, J.B. Miller, A.J. Gellman, High-throughput characterization of early oxidation across $Al_xFe_yNi_{1-x-y}$ composition space, Corros. Sci. 91 (2015) 46–57, https://doi.org/10.1016/j.corsci.2014.10.034.
[35] M.A. Payne, J.B. Miller, A.J. Gellman, High-throughput characterization of the effects of H_2O vapor on early oxidation across $Al_xFe_yNi_{1-x-y}$ composition space, Corros. Sci. 106 (2016) 61–81, https://doi.org/10.1016/j.corsci.2016.01.026.

[36] M.A. Payne, J.B. Miller, A.J. Gellman, High-throughput screening across quaternary alloy composition space: oxidation of $(Al_xFe_yNi_{1-x-y})_{\sim 0.8}Cr_{\sim 0.2}$,, ACS Comb. Sci. 18 (2016) 559–568, https://doi.org/10.1021/acscombsci.6b00047.

[37] R.M. Luna-Sánchez, I. González-Martínez, Combinatorial fabrication and characterization of oxide and metal thin film composition spreads, ECS Trans. 2 (2019) 79–90, https://doi.org/10.1149/1.2193876.

[38] Z. Qiao, Z. Wang, C. Zhang, S. Yuan, Y. Zhu, J. Wang, Perspective high-throughput methods using composition and structure spread libraries, AIChE J. 59 (2012) 215–228, https://doi.org/10.1002/aic.

[39] M.A. Payne, J.B. Miller, M.E. Oliveros, G. Perez, C.P. Gouvea, B.S. Archanjo, C. A. Achete, A.J. Gellman, Assessment of a high-throughput methodology for the study of alloy oxidation using $Al_xFe_yNi_{1-x-y}$ composition gradient thin films, ACS Comb. Sci. 18 (2016) 425–436, https://doi.org/10.1021/acscombsci.6b00030.

[40] D. Priyadarshini, P. Kondratyuk, J.B. Miller, A.J. Gellman, Compact tool for deposition of composition spread alloy films, J. Vac. Sci. Technol. A 30 (2012), https://doi.org/10.1116/1.3664078.

[41] B. Fleutot, J.B. Miller, A.J. Gellman, Apparatus for deposition of composition spread alloy films: the rotatable shadow mask, J. Vac. Sci. Technol. A (2012), https://doi.org/10.1116/1.4766194.

[42] J.I. Goldstein, D.E. Newbury, J.R. Michael, N.W.M.M. Ritchie, J.H.J. Scott, D. C. Joy, Scanning Electron Microscopy and x-Ray Microanalysis (2017), https://doi.org/10.1007/978-1-4939-6676-9.

[43] J. Colligon, Surface modification by ion beams, Vacuum 36 (1986) 413–418, https://doi.org/10.1016/0042-207X(86)90218-6.

[44] I.K. Averkiev, O.R. Bakieva, O.M. Nemtsova, A.A. Kolotov, F.Z. Gil'mutdinov, Changes in the chemical compound and local atomic structure of ultrathin surface layers of Fe due to implantation of argon and oxygen ions, Appl. Surf. Sci. 539 (2021) 148243, https://doi.org/10.1016/j.apsusc.2020.148243.

[45] I.N. Demchenko, Y. Melikhov, Y. Syryanyy, I. Zaytseva, P. Konstantynov, M. Chernyshova, Effect of argon sputtering on XPS depth-profiling results of Si/Nb/Si, J. Electron. Spectros. Relat Phenomena 224 (2018) 17–22, https://doi.org/10.1016/j.elspec.2017.09.009.

[46] G. Greczynski, L. Hultman, Towards reliable X-ray photoelectron spectroscopy: sputter-damage effects in transition metal borides, carbides, nitrides, and oxides, Appl. Surf. Sci. 542 (2021) 148599, https://doi.org/10.1016/j.apsusc.2020.148599.

[47] R. Steinberger, J. Duchoslav, M. Arndt, D. Stifter, X-ray photoelectron spectroscopy of the effects of Ar^+ ion sputtering on the nature of some standard compounds of Zn, Cr, and Fe, Corros. Sci. 82 (2014) 154–164, https://doi.org/10.1016/j.corsci.2014.01.018.

[48] S. Hofmann, Y.S. Han, J.Y. Wang, Depth resolution and preferential sputtering in depth profiling of sharp interfaces, Appl. Surf. Sci. 410 (2017) 354–362, https://doi.org/10.1016/j.apsusc.2017.03.110.

[49] T.J. Chuang, C.R. Brundle, K. Wandelt, An X-ray photoelectron spectroscopy study of the chemical changes in oxide and hydroxide surfaces induced by Ar^+ ion bombardment, Thin Solid Films 53 (1978) 19–27, https://doi.org/10.1016/0040-6090(78)90365-6.

[50] R. Steinberger, J. Walter, T. Greunz, J. Duchoslav, M. Arndt, S. Molodtsov, D. C. Meyer, D. Stifter, XPS study of the effects of long-term Ar^+ ion and Ar cluster sputtering on the chemical degradation of hydrozincite and iron oxide, Corros. Sci. 99 (2015) 66–75, https://doi.org/10.1016/j.corsci.2015.06.019.

[51] E.F. Smith, J.D.P. Counsell, J. Bailey, J.S. Sharp, M.R. Alexander, A.G. Shard, D. J. Scurr, Sample rotation improves gas cluster sputter depth profiling of polymers, Surf. Interface Anal. 49 (2017) 953–959, https://doi.org/10.1002/sia.6250.

[52] F. Weng, S. Gao, J. Jiang, J.J. Wang, P. Guo, A novel strategy to fabricate thin 316L stainless steel rods by continuous directed energy deposition in Z direction, Addit. Manuf. 27 (2019) 474–481, https://doi.org/10.1016/J.ADDMA.2019.03.024.

[53] P. Boillot, J. Peultier, Use of stainless steels in the industry: recent and future developments, Procedia Eng. 83 (2014) 309–321, https://doi.org/10.1016/J.PROENG.2014.09.015.